On the control of the first Bragg band gap in periodic continuously corrugated beam for flexural vibration

Adrien Pelat, Thomas Gallot, François Gautier

On the control of the first Bragg Band gap in periodic continuously corrugated beam for flexural vibration

Adrien Pelat, Thomas Gallot, François Gautier

Laboratoire d'Acoustique de l'Université du Mans, CNRS, Av. Olivier Messiaen, 72085 Le Mans, FRANCE

Instituto de Física, Universidad de la República de Uruguay, Montevideo, URUGUAY

Abstract

This work aims to provide better physical understanding of Bragg band gap effects in continuously periodic corrugated beams for flexural waves. The main outcome is the establishement of original algebraic formulas for the band gap width and central frequency. It is shown that the band gap width and central frequency only depend on a thickness contrast parameter. To do so, a so called *two-skins* geometry is proposed to approximate the usual solid beam cross section, in order to greatly simplify analytical derivations following the Plane Wave Expansion (PWE) method applied to Euler-Bernoulli theory. Theoretical predictions in the *two-skins* geometry successfully match the results in the practical case of a solid geometry obtained from both experiments on a beam demonstrator and numerical simulations done by classical PWE (1D Euler and Timoshenko theories) or finite element (3D elasticity theory) methods. The complete set of results is benchmarked in details so that the geometrical approximation is validated and the algebraic formulas are usable as design tools of such notch filters. Moreover, flexural and longitudinal motion coupling due to the non-symetrical thickness profile of the demonstrators leads to an additional band gap that is experimentally identified. A numerical study illustrates the resulting double filtering effect. Potential applications of the background provided by this work can concern Noise,Vibration and Harshness (NVH) engineering, for which meta-materials can be very relevant especially when structure lightening is required.

Keywords: Bragg band gaps, flexural waves, periodic corrugated beam, wave coupling, design tools
PACS: code, code
2000 MSC: code, code

1. Introduction

Meta-materials are extensively studied for the last decades in many fields of wave physics for their attractive ability to control unusual wave propagation properties [1, 2, 3]. In most cases they are designed as periodic and/or locally resonant propagation media from which typical applications concern wave filtering, guiding, lensing and cloaking.

In the context of mechanical engineering, the use of meta-materials for mitigating noise and vibration appears as a promising technique particularly when lightweigthing of industrial structures is a central issue [4]. In that purpose, a main challenge is to reach attractive mitigation performances even in the low frequency range for which the wavelength and the finite size of the structure of interest are in the same range. Another challenge is to achieve to tune band gaps location and bandwidth to match an expected mitigation template corresponding to a given application. In most cases, a particular attention is paid to flexural waves because of their major contribution to the structure born sound.

The design of such structures then require to well understand how the wave propagation properties can be tailored from the local geometrical and material settings of the unit cell. This leads to many open questions for which the literature is very extensive. Among many others, some of the recent works typically focus on the optimization of periodic Euler-Bernoulli beams from Transfer Matrix Method [5], Plane Wave Expansion Method [6], Waveguide Finite Element method [7] or varying amplitudes method [8].

The insertion of local resonances also leads to many architected layouts leading to structures that efficiently open band gaps [9, 10, 11, 12, 13, 14, 15, 16].

In the case of thick beams compared with the wavelength, the effects of the rotational inertia and shear deformation must be described using Timoshenko theory [17, 18, 19, 20, 21, 22, 23, 24].

Periodic pipes and cylindrical shells are also of great interest in some industrial applications, they are the subject of shape optimization from Floquet theory [25] and imply to take into account the fluid/structure interaction [26, 27, 28].

In the case of sophisticated designs of periodic and locally resonant structural waveguides, 1D beam theories become unadapted and can be replaced by 3D elasticity numerical models solved by using finite element based methods [29, 30, 31, 32]. For more details, the reader can refer to the above cited articles and related references.

Most of the time, the involved geometrical and material designs of these taylored system are quite complex and make uneasy to establish some general links between the band gap features and the unit cell design parameters. By the way, some numerical parametric variations as in [5] illustrate possible tendencies.

The main goal of this work is to provide better physical understanding of vibration filtering properties of continuously periodic beams by deriving an analytical model of the Bragg band gap of flexural vibrations. The structure of interest whose unit cell is represented in Fig.1(a), is a corrugated beam with a geometrical layout close to the one studied in [33]. Following the same thickness profile, a so-called *two-skins* geometry that approximates the solid geometry is also proposed. The interest of this theoretical geometry is to enable to achieve complete analytical derivations following the PWE method applied to the Euler-Bernoulli framework. From this, simple and cost free design tools able to predict the Bragg band gap features are proposed.

The article is structured as follows. PWE method is recalled in section 2.1. The corrugated thickness profile of the studied beams is defined in section 2.2. Analytical derivations based on the PWE method applied to the case of an approximated two-skins geometry are presented in section 2.3. In section 3 an experimental study that also involves comparisons with other PWE and FE numerical simulations : the demonstrators, the experimental setup and the results analysis are presented in section 3.1, 3.2 and 3.3, respectively.

2. Model of the central frequency and width of the first band gap

2.1. Plane wave expansion for an Euler-Bernoulli periodically corrugated beam

Under Euler-Bernoulli assumptions and considering harmonic motion proportional to the implicit time factor $\mathrm{e}^{j\omega t}$, the free flexural displacement $w(x)$ in a beam of variable thickness $h(x)$ and uniform width b obeys the equation of motion

$$-\rho_L(x)\omega^2 w(x) + \frac{\partial^2}{\partial x^2} D(x) \frac{\partial^2 w(x)}{\partial x^2} = 0, \tag{1}$$

where $\rho_L(x)$ is the linear density and $D(x)$ is the beam flexural stiffness, both depending on the section geometry.

The beam is supposed to be an infinite periodic distribution of a unit cell of size L. As a consequence, the mechanical properties are periodic functions of space and can be expanded as the following Fourier series :

$$\rho_L(x) = \sum_{g_2} \alpha_{g_2}(k) \mathrm{e}^{\mathrm{j}g_2 x} \quad \text{and} \quad D(x) = \sum_{g_2} \delta_{g_2}(k) \mathrm{e}^{\mathrm{j}g_2 x} \tag{2}$$

where $g_2 = \dfrac{n_2 2\pi}{L}$, n_2 being an integer and where the Fourier coefficients α_{g_2} and δ_{g_2} are defined by $\alpha_{g_2} = \dfrac{1}{L}\int_0^L \rho_L(x)\mathrm{e}^{-\mathrm{j}g_2 x}\mathrm{d}x$, $\delta_{g_2} = \dfrac{1}{L}\int_0^L D(x)\mathrm{e}^{-\mathrm{j}g_2 x}\mathrm{d}x$.

According to the Bloch theorem [4], the solution of Eq.(1) is sought as the following series

$$w(x) = \sum_{g_1} w_{g_1}(k) \mathrm{e}^{\mathrm{j}g_1 x} \mathrm{e}^{\mathrm{j}kx}, \tag{3}$$

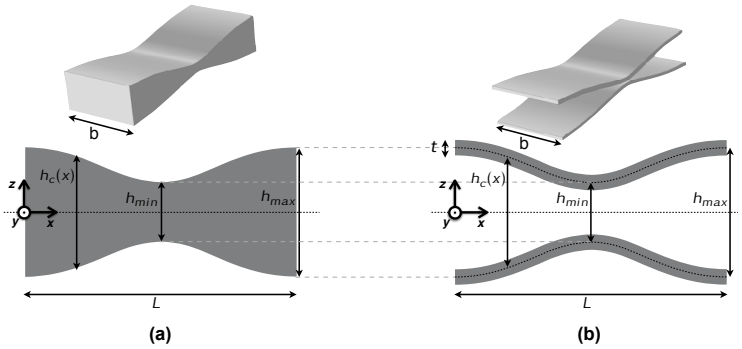

Figure 1: Views and detailed sketches of a unit cell of the studied periodic corrugated beams. The profile geometry is described in Eq.(6) : (a) case of a solid cross section (b) case of a two-skins geometry

where k is the flexural wavenumber and $g_1 = \dfrac{n_1 2\pi}{L}$, n_1 being an integer.

Truncating the Fourier series (2) (by considering $n_2 \in [-N_2; N_2]$) and the plane wave expansion (3) (by considering $n_1 \in [-N_1; N_1]$), the equation of motion (1) turns to an eigenproblem

$$(\mathbf{P}(k) - \omega^2 \mathbf{Q})\mathbf{W} = \mathbf{0}, \tag{4}$$

where $\mathbf{W}$ is the $(2N_1 + 1, 1)$ column vector composed of the coefficients $w_{g_1}(k)$. The size of matrices $\mathbf{Q} = (Q_{n_3 n_1})$ and $\mathbf{P} = (P_{n_3 n_1})$ is $(2N_3 + 1, 2N_1 + 1)$, with $N_3 = N_1 + N_2$. The generic terms $Q_{n_3 n_1}$ and $P_{n_3 n_1}$ are given by $Q_{n_3 n_1} = \alpha_{g_3 - g_1}$ and $P_{n_3 n_1}(k) = \delta_{g_3 - g_1}(k+g_1)^2(k+g_3)^2$. Solving the generalized eigenvalue problem (4) provides the circular frequency ω numerically for any given wavenumber k. For this reason, the method is called a $\omega(k)$ method.

Considering the first term in the Fourier series corresponding only to $n_1 = 0$, and $n_3 = 0$, Eq.(4) yields interestingly to the well known dispersion curve : $\omega^2 = k^4 \bar{D}_0$ with the specific flexural stiffness $\bar{D}_0 = \frac{\delta_0}{\alpha_0}$. In this case, the homogeneous-equivalent behavior is captured by the specific flexural stiffness at the first order of the Fourier series. Note that for a prismatic beam with a rectangular solid cross section, this specific flexural stiffness is given by

$$\bar{D}(x) = \frac{D(x)}{\rho_L} = \frac{E h^2(x)}{12\rho}, \tag{5}$$

with h the beam thickness, E the material Young's modulus, ρ is the material density related to the linear density by $\rho_L = \rho h b$.

2.2. Thickness profile of the beam

The studied system is an infinite periodic beam whose thickness is defined by

$$h(x) = h_o\sqrt{1 + C.cos\left(\frac{2\pi x}{L}\right)}, \tag{6}$$

where the mean thickness h_0 and the contrast parameter C can be related to the maximum and minimum thicknesses, respectively h_{max} and h_{min} (see Fig.1(b)):

$$h_0^2 = \frac{h_{max}^2 + h_{min}^2}{2}, \tag{7a}$$

$$C = \frac{h_{max}^2 - h_{min}^2}{h_{max}^2 + h_{min}^2}. \tag{7b}$$

The contrast parameter is in the range $C \in [0; 1[$, $C = 0$ corresponding to a beam of uniform thickness. Since the thickness cannot be zero, the maximum contrast $C = 1$ cannot be reached but remains $C < 1$.

Based on this profile, two different beam cross sections can be defined, as depicted in Fig.1. The first one is the usual solid cross section (Fig.1(a)) from which the experimental demonstrators defined in section 3.1 are based. The second one (Fig.1(b)) is called *two-skins* approximated geometry. It corresponds to the cross section of a sandwich material made with two stiff skins of thin thickness t spread by a lightweight core of thickness $h(x)$ whose stiffness and mass are ignored. These assumptions could be reached with a honeycomb core typically. This two-skins approximation of the solid case leads to greatly simplify mathematical derivations in order to solve Eq.(4). Indeed, the linear mass of the two-skins cross-section is constant $\rho_L(x) = \rho 2tb$ and does not depend on the profile $h(x)$. Hence, the spatial spectrum of specific flexural stiffness contains only 3 components ($N_2 = 1$).. Considering that t is small compared to h_0, $\bar{D}(x)$ is given by

$$\bar{D}(x) = \frac{Eh_o^2}{4\rho}\left[1 + C.cos\left(\frac{2\pi x}{L}\right)\right] . \tag{8}$$

This property will be exploited in section 2.3 to get an analytical model of the dispersion curves.

PWE numerical computations show that a Bragg band gap opens with the thickness profile of Eq.(6) for both solid and two-skins cases. A convergence study on the truncation level N_1 has been carefully led and shows that the band gap features are well predicted with $N_1 \geq 2$ in both two geometrical cases : with $N_1 = 2$, the error is 1.1% for $C = 0.9$ and 0.008% for $C = 0.6$ in the two-skins case, for example. The convergence rate for solid geometry is roughly the same. Consequently, the following analytical derivations based on the two-skins geometry are done with $N_1 = 2$. $N_1 = 10$ is chosen for all other numerical PWE simulations, which leads to calculation times of a few seconds using a

laptop computer. Note that for all numerical PWE simulations in the case of solid geometry, the truncation $N_2 = 10$ is used and causes a negligible error.

2.3. Dispersion curves and analytical derivation of the first band gap properties

In this section we derive an approximated analytical model of the Bragg band gap to study two features of the resulting filter : the frequency width and the center frequency. Using the PWE formalism presented section 2.1, these band gap features are obtained from the difference and average of the first two eigen frequencies calculated with $k = \pi/L$. These quantities can be computed numerically for any geometry but there is no analytical expression of the eigen frequencies for an arbitrary geometry. However, an approximated analytical solution is established below for the two-skins geometry.

For the two-skins geometry, the linear mass being constant, the mass matrix $\mathbf{Q}$ of Eq.(4) is simply $\mathbf{Q} = \alpha_0 \mathbf{I}$, with $\alpha_0 = 2\rho t b$ and $\mathbf{I}$ the identity matrix. Hence, considering $k = \pi/L$, Eq.(4) becomes

$$\sum_{n_1} \left[\delta_{n_3 - n_1} \left(\frac{\pi}{L} + \frac{2n_1\pi}{L} \right)^2 \left(\frac{\pi}{L} + \frac{2n_3\pi}{L} \right)^2 \right] w_{n_1}(k) - \alpha_0 \omega^2 w_{n_3}(k) = 0, \quad \forall n_3. \tag{9}$$

Defining the dimensionless frequency parameter $X = \frac{\omega^2}{\omega_0^2}$ with $\omega_0^2 = \bar{D}_0 \frac{\pi^4}{L^4}$ the Bragg frequency of the equivalent beam of uniform thickness h_0, it can be rewritten as

$$\sum_{n_1} \left[\bar{\delta}_{n_3 - n_1} (2n_1 + 1)^2 (2n_3 + 1)^2 \right] w_{n_1}(k) - X w_{n_3}(k) = 0, \ \ \forall n_3 = n_1 + n_2, \tag{10}$$

where $\bar{\delta}_n = \frac{\delta_n}{\alpha_0 \delta_0}$. The specific flexural stiffness of Eq. (8) for the two-skins geometry (Fig.1(b)) is described by only three nonzero Fourier coefficients : $\bar{\delta}_0 = 1$, $\bar{\delta}_1 = \bar{\delta}_{-1} = \frac{C}{2}$. Consequently, in the matricial form of Eq. (10), the $(2N1 + 3) \times (2N1 + 1)$ matrix $\mathbf{M} = (\mathbf{P}(k) - \omega^2 \mathbf{Q})$ is tridiagonal but the generalized eigenvalue problem is overconditionned with 2 equations more than unknowns. For the sake of the forthcoming analytical derivations, the first and last equations corresponding to high Fourier components $n_3 = \pm(N_1 + 1)$ are removed, introducing no error for lower component of W. Modified Eq.(10) becomes a classical eigenvalue problem where the square matrix M reads:

$$M = \begin{bmatrix} a_{-N_1} & b_{-N_1} & & & & & \\ b_{-N_1} & a_{-N_1+1} & \ddots & & & & \\ & \ddots & \ddots & b_0 & & & \\ & & b_0 & a_0 & \ddots & & \\ & & & \ddots & \ddots & b_{N_1-1} & \\ & & & & b_{N_1-1} & a_{N_1} & \end{bmatrix}, \tag{11}$$

with $a_n = (2n+1)^4 - X$ and $b_n = (2n+1)^2 (2n+3)^2 \frac{C}{2}$. Apart from the dimensionless frequency parameter X, the matrix M only depends on the contrast parameter C, which already indicates its major influence in the control of the band gap features.

The PWE problem consists then in solving $\det(M) = 0$. The determinant of a tridiagonal matrix can be given by a recurrence relation [34] defined by

$$\theta_n = a_n \theta_{n-1} - b_{n-1}^2 \theta_{n-2} \ , \quad \forall n \in [-N_1 + 1; N_1] \, , \tag{12}$$

and initialized by $\theta_{-N_1-1} = 1$ and $\theta_{-N_1} = a_{-N_1}$. As a result, $\det(M) = \theta_{N_1}$ is a polynomial of order $2N_1 + 1$ of variable X, written as

$$\det(M) = \sum_{n=0}^{1+2N_1} P_n X^n \ , \tag{13}$$

where each P_n is a polynomial of variable C. The first band gap is reached in the vicinity of $X = 1$. Around this value and considering $N_1 = 2$ as suggested by the convergence study, the variations of $\det(M)$ are plotted in black in Fig.2 and exhibit local roots. Analytical solutions of $\det(M) = 0$ are derived from the 5th degree polynomial $\det(M)$ approximated by a 2nd degree polynomial $A(X)$ (see Appendix A for details):

$$A(X) = P_2 X^2 + P_1 X + P_m, \quad \text{with} \quad P_m = \left(\sum_{n=3}^{1+2N_1} P_n + P_0 \right). \tag{14}$$

The validity of the second order approximation $\det(M) \approx A(X)$ in the vicinity of $X = 1$ is verified in Fig.2 where the variations of $\det(M)$ and $A(X)$ according to X are very close each other for three typical values of the contrast parameter C. Fig.2 also verifies that in the case of a beam of uniform thickness ($C = 0$), the two degenerated roots equal to $X = 1$, no band gap is open on the Bragg frequency ω_0. When the contrast parameter increase ($C > 0$), the parabola exhibits two single roots around $X = 1$. In the following, the relative spread and mean value of the two roots are derived analytically to study the links between contrast C and the band gap features.

The average $\bar{X}$ and difference $\mathrm{d}X$ between the two roots of $A(x)$ are given by:

$$\bar{X} = -\frac{P_1}{2P_2}, \tag{15a}$$

$$dX = \frac{\sqrt{P_1^2 - 4P_m P_2}}{P_2}. \tag{15b}$$

Substituting Eqs.(15) into the differential $\frac{\mathrm{d}f}{f_0} = \frac{\mathrm{d}X}{2\sqrt{\bar{X}}}$ obtained from the definition $X = \omega^2/\omega_0^2$ easily leads to

$$\frac{\mathrm{d}f}{f_0} = \sqrt{\frac{4P_m P_2 - P_1^2}{2P_1 P_2}}. \tag{16}$$

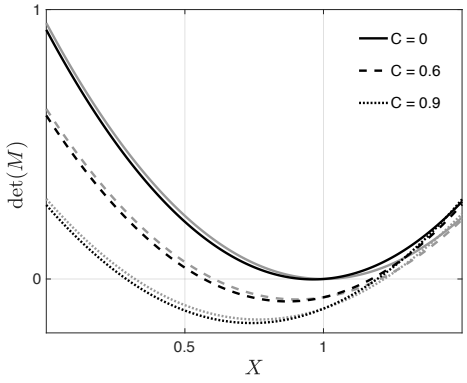

Figure 2: Variations at the vicinity of the normalized frequency $X = 1$ of the fifth order polynomial $\det(M)$ (gray, corresponds to Eq.(13) with $N_1 = 2$) and second order approximation $A(X)$ (black, corresponds to Eq.(14). The roots provides the eigen frequencies and so the band gap limits for $C = 0$ (full line), $C = 0.6$ (dashed line), $C = 0.9$ (dotted line).

Substituting Eq.(14) in Eq.(16) with $N_1 = 2$ provides after a few algebra the following formula for the relative band gap width (See **??** for details):

$$\frac{\mathrm{d}f}{f_0} \approx \frac{C}{2}\left(\frac{1-\frac{1}{2}C^2}{1-\frac{3}{4}C^2}\right)^{1/2}. \tag{17}$$

Similarly, substituting Eq.(14) in Eq.(15a) gives an algebraic formula for the band gap central frequency:

$$\frac{f_c}{f_0} \approx \left(\frac{1-\gamma C^2}{1-\beta C^2}\right)^{1/2}, \tag{18}$$

with $\gamma = \frac{1}{2}$ and $\beta = \frac{1}{4}$.
Fig.3(a) plots the relative band gap width $\mathrm{d}f/f_0$ as a function of the contrast C. A very good agreement is found between numerical PWE for the two-skins geometry (green circles), analytical expression for the two-skins geometry (Eq. (17)) (full line), and numerical PWE for the solid geometry (green dots). Three main interpretations results from this agreement. First, two-skins geometry is a very good approximation of the solid geometry to estimate the band gap width. Only a slight drift occurs for very large contrast values : the error becomes greater than 1% for $C > 0.82$ (see green dots and circles). Second, the band gap width is essentially driven by the flexural stiffness contrast and does not depend on the linear mass contrast. Indeed, whether the linear mass is considered constant (in the two-skin case) or not (in the solid case), results are the same. Third, the second order approximation of $det(M) = 0$ that leads to formula (17) provides a very accurate model of the band gap width : the induced error is particularly small compared to the numerical result (see full line and green circles).

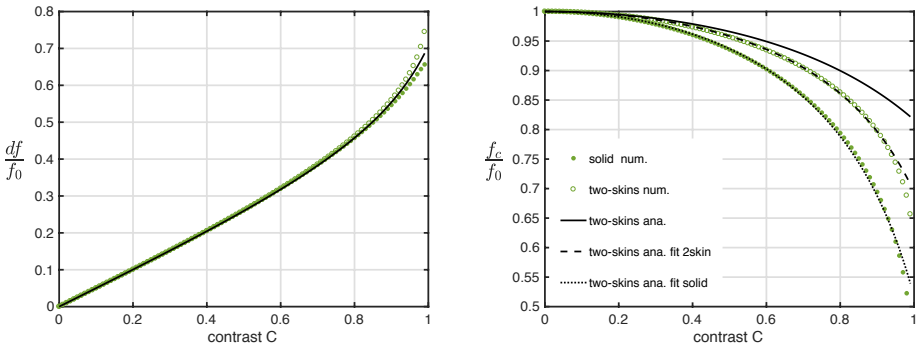

Figure 3: Variations versus contrast parameter C of (a) the relative width df/f_0 and (b) the relative central frequency fc/f_0 of the Bragg band gap obtained from formulas (17-18) (full line) and numerical PWE simulations for the solid (green dots) and two-skins (green circles) geometries. The plot fc/f_0 also displays the formula (18) fitted to either the two-skins (dashed line, $\gamma = 0.73; \beta = 0.44$) or solid (dotted line, $\gamma = 0.8; \beta = 0.40$) geometries.

However, concerning the central frequency, Fig.3(b) shows that the two-skins geometry is only valid for low contrast values : the error becomes $> 2\%$ from $C \geq 0.5$ (see drift between green points and circles). This significant difference indicates that the band gap central frequency is sensitive to contrasts in flexural stiffness on the one hand, but also in linear mass that is not taken into account in the two-skins geometry. In addition, the parabolic approximation introduces an additional error (see difference between full line and green circles), which restricts the use of the formula (18) : the estimation error of f_c is more than 1% from $C > 0.3$ (see drift between full line and green dots). Hence, to more accurately estimate f_c, the coefficients β and γ are recomputed by minimizing a cost function: $\epsilon(\beta, \gamma) = \left(\frac{1-\gamma C^2}{1-\beta C^2}\right)^{1/2} - f_{N_1=20}$. These fits of the analytical expression Eq. (18) to the PWE simulations of either the two-skins (dashed line, $\beta = 0.44$ and $\gamma = 0.73$) or solid (dotted line, $\beta = 0.4$ and $\gamma = 0.8$) are shown in Fig.3(b). In some way, this correction partly corresponds to an artificial consideration of the linear mass effects that are not described by the two-skins geometry. The good agreement after correction indicates that the model captures qualitatively well the phenomena of interest. Note that in the benchmark of Tab.1 and Fig.7, the results labeled "two-skins analytical model" refer to Eq.(17) and Eq.(18) fitted to the solid geometry, that is with $\beta = 0.4$ and $\gamma = 0.8$.

3. Experimental study of practical demonstrators

3.1. Demonstrators design and manufacturing

Two experimental beam demonstrators are manufactured from homogeneous aluminum bars of width $b = 80$mm. Both demonstrators have 8 cells with the

thickness profile defined in Eq.(8). The unit cell length is $L = 180$mm such that the total length is $L_{tot} = 1440$mm. The most contrasted beam, called "Beam A", has a contrast $C = 0.88$ with $h_{max} = 20$mm and $h_{min} = 5$mm while the "Beam B" has a contrast $C = 0.6$ with $h_{max} = 18.44$mm and $h_{min} = 9.22$mm. The material parameters are $E = 70$GPa and $\rho = 2700\text{kg}/\text{m}^2$. An aluminum beam of uniform thickness $h = 20$mm with same total length and width is also studied as a reference.

All beams are manufactured by conventional machining using a Computer Numerical Control (CNC) milling machine. For manufacturing convenience, only the top surface of the beams is machined as seen on the Computer assisted Design (CAD) view in Fig.4(a). The values of the thicknesses and contrast defined above are respected, but the thickness profile as shown in the Fig.1(a) is no longer symmetrical. The effect of such a non-symmetrical manufacturing is discussed based on the results of Fig.6.

3.2. Experimental setup and data processing

The experimental setup view shown in Fig.4 is a classical scanning laser vibrometer setup. The demonstrator is vertically hung from a rigid frame to approximate the free boundary conditions. A shaker placed at the the demonstrator lower end excites flexural motion. The propagation of torsional waves is limited by applying the excitation on the center of the beam width. The driving signal is a periodic chirp in the [0-6.15]kHz frequency range with a 976 mHz frequency step. A force sensor measures the driving force at the excitation point. A scanning laser vibrometer (Polytech PSV 500) measures the out-of-plane motion of the demonstrator over a $N = 4215$ points Cartesian mesh with a 5 mm space step (281 lines and 15 columns). An average over 3 signal samples is set for all acquisitions to increase signal to noise ratio.

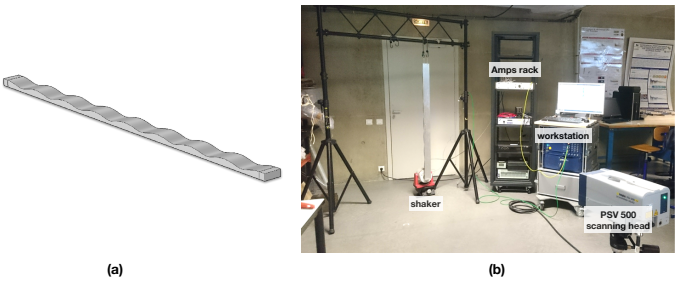

Figure 4: A picture of the experimental set up shows a suspended 8-cell corrugated beam driven by a shaker at the bottom end. A laser vibrometer measures the out of plane component of the particle velocity on 4215 points distributed over the whole vibrating structure.

For every mesh point of coordinate (x, y), with x the axial coordinate, y the

transverse coordinate, f the frequency, the mobility transfer function

$$Y(x, y, f) = \frac{V(x, y, f)}{F(f)} \tag{19}$$

is measured. $V(x, y, f)$ the local out-of-plane velocity and $F(f)$ the driving force at the excitation point. Therefore, the flexural field $Y(x, y, f)$ along the whole beam is represented for selected frequencies in Fig.5(a) and (d). To minimize the amplitude of torsional movement, $\bar{Y}(x, f)$ is calculated as the average of $Y(x, y, f)$ over the beam width. The whole experimental data set corresponding to a beam demonstrator can then be represented as a map as in Fig.5(b) and (e). Each line of such a map corresponds to a transfer function at a selected point while each column is an operational shape at a selected frequency. In order to provide a frequency response independent from a given observation point, the space averaged square mobility $< Y >$ is calculated as

$$< Y(f) >= \sqrt{\frac{1}{S}\sum_{i}^{N} Y_i^2} \quad , \tag{20}$$

and is shown in Fig.5(c) and (f).

The wavenumber maps $Y(k, f)$ represented in Fig.6(a), (b) and (c) are obtained from a one dimensional x-coordinate space Fourier transform of $\bar{Y}(x, f)$. Signals are Hamming windowed and zero padded to $2^{11} = 65536$ FFT lines in total, resulting in a $dk = 0.02\text{m}^{-1}$ wavenumber step. For each frequency, the maximal value of $|Y(k, f)|$ is extracted (black dots) to identify the experimental dispersion curve folded in the range $kL = [0 - 1]$ in Fig.6(d), (e) and (f).

3.3. Results analysis

The reference beam exhibits an expected classical modal behavior in Fig.5(f). In addition to the series of free-free beam flexural peaks, spurious modes appear at 1666Hz, 3444Hz and 5138Hz (see Fig.5(d) at 1666Hz, for example). These modes are not due to torsional motion because of their non harmonic modal frequencies but may correspond to uncontrolled defaults of the overall mechanical installation.

More remarkably, the beam A with a $C = 0.88$ (high contrast beam) exhibits two frequency ranges with a strongly attenuated field (Fig.5(b), green and red patches). In these ranges that correspond to a band gap (as discussed below), the beam is non resonant and displays only evanescent waves from the excitation point (Fig.5(a) at 700Hz, for example).

The analysis of the experimental dispersion relations in Fig.6 is led from comparisons with the results from three numerical models of infinite periodic solid beams:

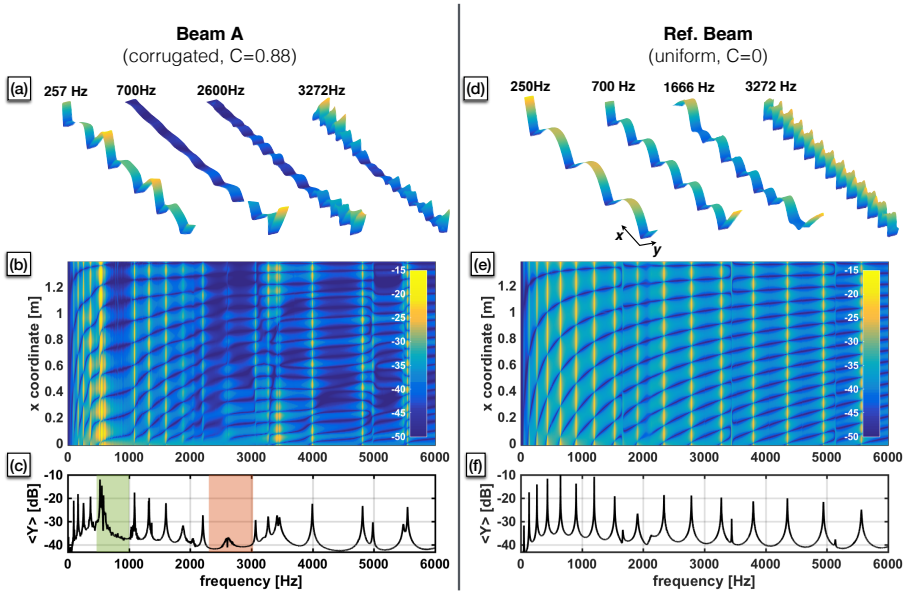

Figure 5: Experimental transfer functions measured on beam A (left column) and reference beam (right column). Data are represented as operational shapes $Y(x, y)$ at selected frequencies in (a) and (d); maps of mobility $\bar{Y}(x, f)$ in (b) and (e); space averaged square mobility $< Y(f) >$ in (c) and (f).

- 1D Euler-Bernoulli beam model solved with the classical PWE method (green line) as described in section 2.1, applied to the symmetric solid unit cell in Fig.1;
- same as previous but in the framework of 1D Timoshenko beam as described in Appendix B ;
- 3D elasticity model solved with the Finite Element Method (COMSOL package) with periodic Floquet conditions defined at the in/out faces of the unit cell (brown circles), applied to the practical case of the beam demonstrators with non symmetric solid unit cell, as discussed in section 3.1 .

While the 1D models only describe the flexural motion in the z polarization, the 3D model gives all the four different types of motion. The eigen shapes then identify the dispersion branches corresponding to the flexural (z and z polarizations), torsional and longitudinal waves (see Fig.6(f) for the reference beam, for example).

For the reference beam (Fig.6 (c) and (f)), the natural dispersion relation for flexural waves ($k \propto \sqrt{\omega}$ expected by the Euler theory is well experimentally

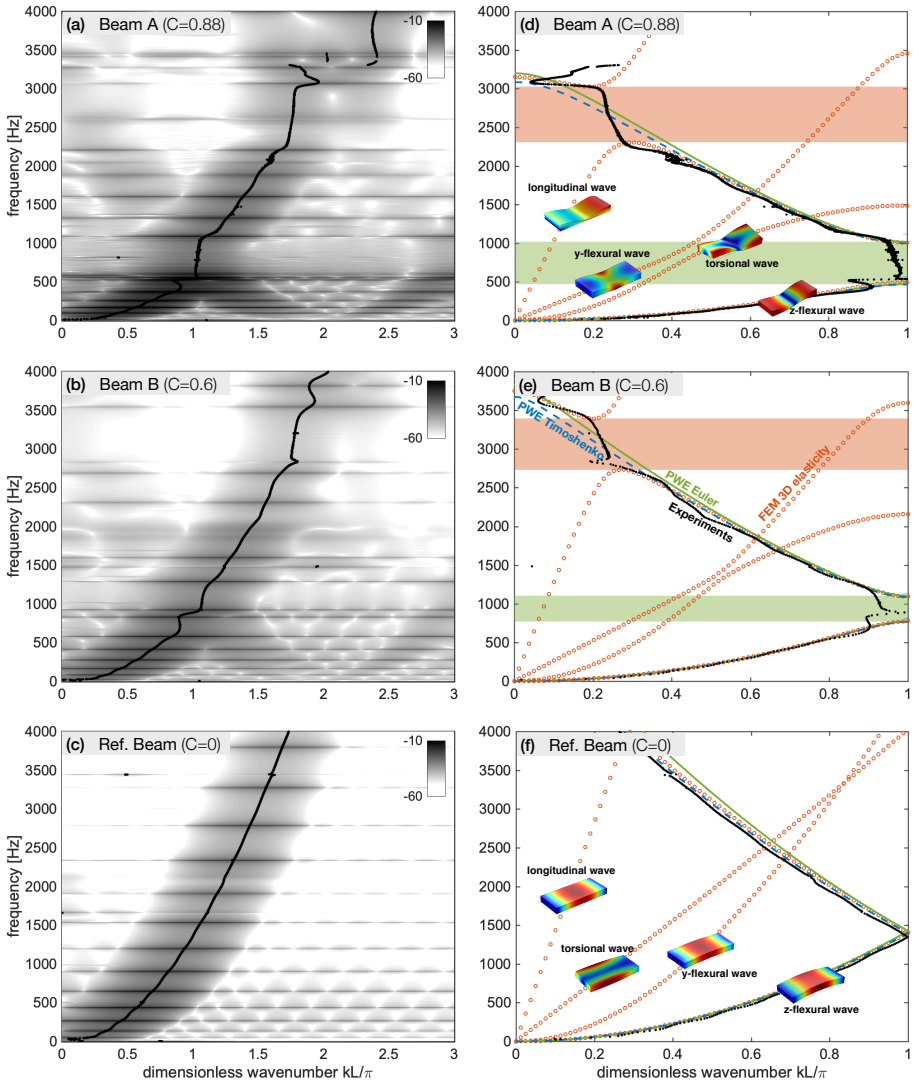

Figure 6: (a-b-c) Experimental wavenumber maps $Y(k, f)$ (modulus in dB scale); (d-e-f) Folded representation of the dispersion relations obtained from experiments (black dots), Euler (green full line) and Timoshenko (blue dashed line) PWE simulations, 3D elasticity FEM simulations (brown circles). Snapshots of the unit cell eigen shapes (FEM) identify the different types of waves. Green patches represent the Bragg band gap obtained from PWE Euler simulations and brown patches represent the flexural/longitudinal coupling band gap obtained from FEM simulations.

recovered. At low frequency ($f < 2$kHz approximately), all the 3 numerical models are in very good agreement with experiments. Beyond, the Euler model

deviates as frequency increases, as expected given the limits of this theoretical low frequency framework. This deviation is significantly smaller with the less restrictive Timoshenko model. 3D elasticity FEM simulations confirm these agreements for flexural waves and also predicts the possible propagation of other wave types that are not involved in the experiments.

The contrasted beams A and B clearly display a band gap for $k = \frac{\pi}{L}$ (6 (d) and (e)). The Bragg band gap as found by the 1D Euler PWE numerical model is represented by the green patch. The agreement is rather better for the beam A of high contrast than for for the less contrasted beam B because of an unexpected resonance within the gap. The destructive interferences occurring within the gap explain the difficulty to well measure the dispersion curves that consequently not perfectly touch the axis $k = \frac{\pi}{L}$ (Fig.6(d) and (e)). However, the dispersion curve is almost vertical in this frequency range, which reflects a quasi-zero group speed that is typical of a band gap. The non perfect vertical layout is attributed to the loss effects, that are not studied here. Outside the gap the agreement between experiment and models is very good.

A detailed quantitative benchmark is proposed in Fig.7 and table 1 to gather all the results obtained for the Bragg band gap with all the four used approaches : two-skins analytical model (after fit on the solid geometry, with $\beta = 0.4$ and $\gamma = 0.8$.), numerical simulations (Euler and Timoshenko numerical PWE models and 3D elasticity FEM with periodic Floquet conditions models for solid geometry) and experimental data.

Fig.7 is a zoom view of the dispersion relations around the Bragg frequency for the beam A (red), beam B (orange) and reference beam (black). For convenient comparison with the two-skins analytical model (color patches with min/max cursors) the frequencies are normalized as in Eq.(17) and (18). In this normalized representation, the agreement between experiments (dots) and models (solid Euler PWE simulations in full lines) results in an alignment of the curves around $f/f_0 = 1$. In particular, analytical and numerical PWE band gaps are almost perfectly superposed. The slight general overestimation of the frequencies observed in the models can be attributed to the poor knowledge on the Young modulus of the demonstrators and manufacturing uncertainties.

In Tab.1 Δf and f_c are defined as $\Delta f = f_{max} - f_{min}$ and $f_c = (f_{max} + f_{min})/2$ with f_{min} and f_{max} the frequency limits of the band gap corresponding to the two first eigenvalues associated to $k = \frac{\pi}{L}$. The extraction of the experimental gap features is less straightforward since the dispersion curves do not exactly touch the axis $k = \frac{\pi}{L}$ (Fig.6(d) and (e)). In this case the frequency peaks surrounding the gap in the wavenumber maps (Fig.6(a) and (b)) are chosen to evaluate f_{min} and f_{max}. The agreement between all results exhibits a maximal error limited to 7.6% (the FEM 3D model as the reference), excepted for experiments of beam B for which a non expected resonance in the gap dis-

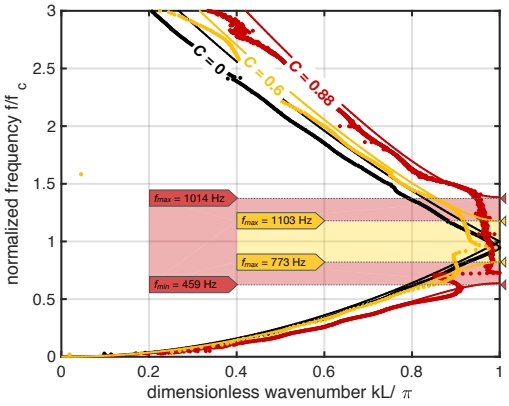

Figure 7: Around the first Bragg frequency f_0, the dispersion curves of the studied beam A (red), beam B (orange) and reference beam (black) obtained from experimental results (dots) are in agreement with the solid beam Euler PWE simulations (full lines) and the two-skins analytical model (color patches with cursors).

Features		Beam A	Beam B	Ref. beam
contrast C		0.88	0.6	0
$[h_{min}; h_{max}]$ (mm)		[5;20]	[9.22;18.44]	[20;20]
Δf (Hz)	two-skins	555 (+7.3%)	330 (+4.1%)	0
	PWE Euler	553 (+7.0%)	333 (+5.0%)	0
	PWE Timo.	533 (+3.1%)	322 (+1.6%)	0
	FEM 3D	517 (ref.)	317 (ref.)	0
	experiments	564 (+3.3%)	365 (+15.1%)	0
f_c (Hz)	two-skins	736 (-2.0%)	938 (+0.3%)	1425 (+1.4%)
	PWE Euler	743 (-1.1%)	938 (+0.3%)	1425 (+1.4%)
	PWE Timo.	736 (-2.0%)	926 (-1.0%)	1396 (-0.7%)
	FEM 3D	751 (ref.)	935 (ref.)	1406 (ref.)
	experiments	808 (+7.6%)	1106 (+18.3%)	1348 (-4.1%)

Table 1: Benchmark table gathering the Bragg band gap features obtained from the two-skins analytical model, solid beam Euler and Timoshenko numerical PWE models, 3D elasticity FEM model with periodic Floquet conditions.

turbs the extracted values. The agreement remains acceptable with a maximal error of about 15%.

Measurements on contrasted beams also show another band gap at the higher frequencies ranges $[2300-3027]$Hz for beam A and $[2700-3300]$Hz for beam B. This gap is not predicted by 1D beam theories PWE simulations but is found in good agreement with a 3D elasticity FEM simulations (brown patch) in Fig.6(d) and (e) for both beams A and B, respectively. A more detailed FEM numerical analysis is provided in Fig.8.

Fig.8(a) shows that this band gap is due to wave coupling between longitudinal and flexural motions, similarly as in [33]. This coupling is identified in Fig.8(a) that compares the dispersion relation obtained in the case of the symmetrical geometry of Fig.1(a) (blue triangles) and the non-symmetrical case

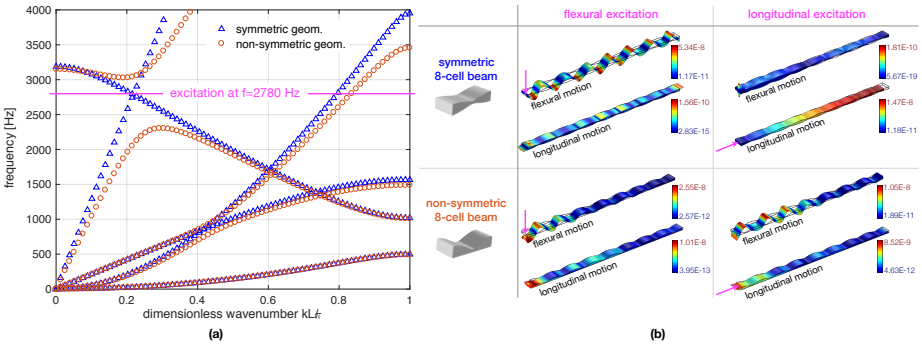

Figure 8: FEM numerical study of the wave coupling band gap and resulting double filtering effect. (a) Comparison of the dispersion relations of a periodic symmetric (blue triangles) and non-symmetric (brown circles) beam ; (b) Flexural and longitudinal components of the forced displacement of a 8-cell beam, symmetrical (top line) or non-symmetrical (bottom line), excited by a flexural (left column) or longitudinal (right column) unit point force (pink arrow) at the coupling frequency $f = 2780$Hz

(brown circles) corresponding to the experimental demonstrator. Both geometrical layouts follow the corrugated profile of Eq.(6) with $h_{max} = 20$mm and $h_{min} = 5$mm. In the symmetrical case at $f = 2768$Hz, the longitudinal and flexural dispersion branches cross each other without inducing any coupling between the two motions, due to the neutral straight line of the symmetric beam. On the contrary, the non-symmetry of the cell leads to a curvature of the neutral line of the beam and induces such a coupling as it is well known in shells. Under 1500Hz below the the coupling band gap, the effects of non-symmetry on the dispersion branches remain very small and therefore the first Bragg band gap, are not modified at all.

Fig.8(b) illustrates the motion coupling and the resulting double filtering effect. The z-flexural and longitudinal components of the displacement field are simulated by classical FEM for free-free beams of 8 symmetric (top line) or non-symmetric (bottom line) cells, excited by a flexural (left column) or longitudinal (right column) unit force, at the coupling frequency $f = 2780$Hz. In the symmetrical case, the component of the displacement in the same orientation as the excitation force exhibits a propagative behaviour while the other component, not excited and not coupled, shows a very low residual amplitude. On the contrary, in the non-symmetrical case, the two components of the displacement are, by coupling, in the same range near the point of force application. Associated with periodicity, the coupling leads to a non propagative wave field for both the two wave types and results in the band gap of significant width in which the beam is non resonant observed in the experiments (left column of Fig.5).

4. Conclusions

This article reports a detailed analysis of the Bragg band gap exhibited in a continuously periodic corrugated beam in order to provide better physical understanding of such vibration filters.The analysis consists firstly in establishing an analytical model of the band gap, secondly in studying beam demonstrators using 3 complementary numerical approaches and an experimental characterization.

The main outcome is the establishment of analytical formulas of the band gap width and central frequency obtained for a so-called *two-skins* geometry chosen in order to simplify PWE derivations. Such cross section corresponds to the one of a sandwich material made with two thin but stiff skins spread by a lightweight but thick core whose stiffness and mass are ignored. Theoretical results shows that the band gap remarkably only depends on a thickness contrast parameter : bandwidth is increasing while central frequency is decreasing with increasing contrast. Moreover, the bandwidth is found to be essentially driven by the stiffness contrast while the central frequency is also sensitive to the linear mass contrast.

A complete benchmark validates the two-skins geometry as a good approximation of the solid geometry as to predict the band gap features. Hence, algebraic formulas provide a simple design tool for flexural waves filters based on such elementary geometry described by a Fourier series of very few terms. The general nature of these formulas is not discussed here. For more complex geometries, very interesting prospects would be to generalize the definition of the property contrast and study its link with band gap features.

Flexural and longitudinal motion coupling due to the non-symmetric thickness profile of the demonstrators opens another band gap at higher frequencies, without modifying the Bragg band gap. The result is a double filter able to mitigate simultaneously the two types of waves, over a significant frequency range. Further works would concern the optimization of such "multi-wave" filters of great potential for application.

Other prospects would take into account structural damping both for modeling by means of the Extended Plane Wave Expansion (EPWE) method [35], and for experimental post-porcessing by means of the SlatCow method [36] able to identify both the real and imaginary parts of the wave number, for exemple.

Aknowledgements

Authors thank Le Mans Université for the invited professor grant that has been awarded to Thomas Gallot for a one month stay that occured in september 2016 to initiate the work. Authors also thank Julien Nicolas and Stanislas Renard who manufactured the demonstrators, and Mathieu Sécail for his fruitfull contribution in the experiments.

Appendix A. Detailed polynomial expressions of df and f_c

This appendix details the expressions of the size and position of the band gap deduced from the analytical expression of the determinant (Eq.(12)) that solves the PWE equations (Eq.(4)). The exact determinant is a polynomial of order $2N_1 + 1$. $A(X)$ approximates the determinant with a parabola around $X = 1$. For $N_1 = 2$ the complete expression of the coefficients of $A(X)$ defined in Eq.(14) are given by:

$$\begin{aligned} P_m &= 3992027 - 4087928C^2 + 12301875C^4 \\ P_1 &= -8309061 + 4168827C^2 - 4157811/16C^4 \\ P_2 &= 4317034 - 1079299C^2. \end{aligned}$$

Substituting these expressions in Eq.(15a) gives:

$$\frac{f_c}{f_0} = \left(-\frac{P_1}{2P_2}\right)^{1/2} \tag{A.1a}$$

$$= \left(\frac{1 - \frac{4168827}{8309061}C^2 + \frac{4157811}{16*8309061}C^4}{1 - \frac{2158598}{8634068}C^2}\frac{8309061}{8634068}\right)^{1/2} \tag{A.1b}$$

$$\approx \left(\frac{1 - 0.501C^2 + 0.031C^4}{1 - 0.250C^2}0.962\right)^{1/2} \tag{A.1c}$$

$$\approx \left(\frac{1 - C^2/2}{1 - C^4/4}\right)^{1/2}. \tag{A.1d}$$

As shown in Figure 2, the main error introduced by the approximation of the determinant by a parabola is its central position: this is clear from Eq. (A.1c) that $\frac{f_c}{f_0}\Big|_{C=0} = 0.962$, instead of 1. This error does not vanish increasing the Fourier truncation number, for instance we have $\frac{f_c}{f_0}\Big|_{C=0} = 0.986$ for $N_1 = 5$. The approximated version of $\frac{f_c}{f_0}$ (Eq. (A.1d)) fix this error and produces less than 0.8% of error compared to (Eq. (A.1b)), interestingly this error does not increase significantly with N_1: for $N_1 = 5$, the error is 1.3%.

For the gap size given by Eq. (17), we limit the size of the expression

discarding insignificant terms in C^6 and C^8:

$$\frac{\mathrm{d}f}{f_0} = \left(\frac{4P_mP_2 - P_1^2}{2P_1P_2}\right)^{1/2} \tag{A.2a}$$

$$= \left(\frac{\frac{27041164812544}{4748079097755136} + C^2 - \frac{2362299612278432}{4748079097755136}C^4 + \mathcal{O}(C^4)}{1 - \frac{5326405753552}{7085530636064}C^2 + \frac{1110370178382}{7085530636064}C^4 + \mathcal{O}(C^4)} \frac{4748079097755136}{2592 * 7085530636064}\right)^{1/2} \tag{A.2b}$$

$$\approx \left(\frac{0.005 + C^2 - 0.497C^4)}{1 - 0.751C^2 + 0.156C^4)}0.258\right)^{1/2} \tag{A.2c}$$

$$\approx \frac{C}{2}\left(\frac{1 - \frac{C^2}{2}}{1 - \frac{3C^2}{4}}\right)^{1/2}. \tag{A.2d}$$

$$\tag{A.2e}$$

The approximated version of $\frac{f_c}{f_0}$ (Eq. (A.2d)) produces less than 6% of error compared to (Eq. (A.2b)), corresponding to extreme an contrast C. Interestingly this error decrease with the Fourier truncation number, for $N_1 = 5$, the error is 4%.

Appendix B. Timoshenko beam PWE model

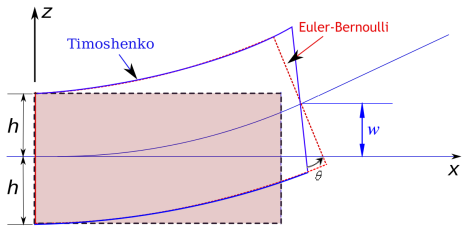

Figure B.9: transversal section deformation of a Timoshenko beam (blue) and an Euler-Bernoulli beam (red). Adapted from *https* : *//en.wikipedia.org/wiki/Timoshenko_beam_theory*

Both Euler Bernouilly and Timoshenko beam vibration theories assume no axial effects (*in-plane* motion) and an undeformable transversal section In order to take into account shear deformation, Timoshenko model allows a rotation of an angle $\theta(x)$ of this section (see Fig.B.9. The equation of motion 1 is replaced by

$$\begin{cases} \frac{\partial}{\partial x}(E(x)I(x)\frac{\partial\theta(x,t)}{\partial x}) + \kappa(x)A(x)G(x)(\frac{\partial w(x,t)}{\partial x} - \theta(x,t)) - \rho(x)I(x)\frac{\partial^2\theta(x,t)}{\partial t^2} & = 0, \\ \kappa(x)A(x)G(x)(\frac{\partial^2 w(x,t)}{\partial x^2} - \frac{\partial\theta(x,t)}{\partial x}) - \rho(x)A(x)\frac{\partial^2 w(x,t)}{\partial t^2} & = 0. \end{cases} \tag{B.1}$$

with A the cross-section area, κ the shear coefficient, I the moment of inertia and $G(x)$ the shear modulus. Since the beam is periodic, properties $m_i(x)$ can be written as Fourrier series:

$$m_i(x) = \sum_{g_2} M_i(g_2) e^{j g_2 x} \tag{B.2}$$

with $m_1(x) = \rho(x)A(x)$, $m_2(x) = \kappa(x)g(x)A(x)$, $m_3(x) = \rho(x)I(x)$ and $m_4(x) = E(x)I(x)$. Furthermore, the beam periodicity imposes a periodicity of both displacement and angle:

$$\begin{aligned} w(x) &= \sum_{g_1} W_k(g_1) e^{j g_1 x}, \\ \theta(x) &= \sum_{g_1} \Theta(g_1) e^{j g_1 x}, \end{aligned} \tag{B.3}$$

As for the Euler-Bernoulli case (see section 2.1), Eq.(B.1) become:

$$\forall g_3 = g_1 + g_2, \forall k \begin{cases} \omega^2 \sum_{g_1} W_k(g_1) = \sum_{g_1} (k+g_1)(k+g_3) M_2(g_3-g_1) W_k(g_1) \\ \qquad\qquad - j(k+g_3) M_2(g_3-g_1)\Theta_k(g_1), \\ \omega^2 \sum_{g_1} M_3(g_3-g_1)\Theta_k(g_1) = \sum_{g_1} [(k+g_1)(k+g_3) M_4(g_3-g_1) \\ \qquad + M_2(g_3-g_1)]\Theta_k(g_1) + j(k+g_1) M_2(g_3-g_1) W_k(g_1), \end{cases} \tag{B.4}$$

The problem can be written in a matrix form by defining a state vector $\mathbf{X}$ as:

$$\mathbf{X} = \left\{ \begin{array}{c} W_k(g_1) \\ \Theta_k(g_1) \end{array} \right\}.$$

Then (B.4) becomes an Eigenvalues problem:

$$\omega^2 \mathbf{P} \mathbf{X} = \mathbf{Q} \mathbf{X} \tag{B.5}$$

where $\mathbf{P}$ and $\mathbf{Q}$ are $[2N_3 + 1 \times 2N_1 + 1]$ matrices:

$$\mathbf{P} = \left[\begin{array}{cc} \mathbf{P_{11}} & \mathbf{0} \\ \mathbf{0} & \mathbf{P_{22}} \end{array} \right], \quad \mathbf{Q} = \left[\begin{array}{cc} \mathbf{Q_{11}} & \mathbf{Q_{12}} \\ \mathbf{Q_{21}} & \mathbf{Q_{22}} \end{array} \right]$$

with

$$\begin{aligned} \mathbf{P_{11}} &= \{P_{11,ij}\}, \quad P_{11,ij} = M_1(g_{3i} - g_{1j}), \\ \mathbf{P_{22}} &= \{P_{11,ij}\}, \quad P_{22,ij} = M_3(g_{3i} - g_{1j}), \\ \mathbf{Q_{11}} &= \{Q_{11,ij}\}, \quad Q_{11,ij} = (k+g_{1j})(k+g_{3i}) M_2(g_{3i} - g_{1j}), \\ \mathbf{Q_{12}} &= \{Q_{12,ij}\}, \quad Q_{12,ij} = -j(k+g_{3i}) M_2(g_{3i} - g_{1j}), \\ \mathbf{Q_{21}} &= \{Q_{21,ij}\}, \quad Q_{21,ij} = j(k+g_{1j}) M_2(g_{3i} - g_{1j}), \\ \mathbf{Q_{22}} &= \{Q_{22,ij}\}, \quad Q_{22,ij} = (k+g_{1j})(k+g_{3i}) M_4(g_{3i} - g_{1j}) + M_2(g_{3i} - g_{1j}). \end{aligned}$$

References

[1] John B Pendry, David Schurig, David R Smith, Controlling electromagnetic fields, science 312 (5781) (2006) 1780–1782.

[2] M. J. Zheng, J. J. Xiao, K. W. Yu, Tunable localization and oscillation of coupled plasmon waves in graded plasmonic chains, Journal of Applied Physics 106 (11) (2009) 113307.

[3] Ming-Hui Lu, Liang Feng, Yan-Feng Chen, Phononic crystals and acoustic metamaterials, Materials Today 12 (12) (2009) 34–42.

[4] D.M. Mead, Wave propagation in continuous periodic structures : research contributions from southampton 1964–1995, Journal of Sound and Vibration 190 (3) (1996) 495–524.

[5] Yanlong Xu, Xiaoling Zhou, Wei Wang, Longqi Wang, Fujun Peng, Bin Li, On natural frequencies of non-uniform beams modulated by finite periodic cells, Physics Letters A 380 (40) (2016) 3278–3283.

[6] Jihong Wen, Gang Wang, Dianlong Yu, Honggang Zhao, Yaozong Liu, Theoretical and experimental investigation of flexural wave propagation in straight beams with periodic structures: Application to a vibration isolation structure, Journal of Applied Physics 97 (11) (2005) 114907.

[7] Niels Olhoff, Bin Niu, Gengdong Cheng, Optimum design of band-gap beam structures, International Journal of Solids and Structures 49 (22) (2012) 3158–3169.

[8] Vladislav S. Sorokin, Jon Juel Thomsen, Eigenfrequencies and eigenmodes of a beam with periodically continuously varying spatial properties, Journal of Sound and Vibration 347 (2015) 14–26.

[9] Yaozong Liu, Dianlong Yu, Li Li, Honggang Zhao, Jihong Wen, Xisen Wen, Design guidelines for flexural wave attenuation of slender beams with local resonators, Physics Letters A 362 (5-6) (2007) 344–347.

[10] Yong Xiao, Jihong Wen, Xisen Wen, Broadband locally resonant beams containing multiple periodic arrays of attached resonators, Physics Letters A 376 (16) (2012) 1384–1390.

[11] Yong Xiao, Jihong Wen, Dianlong Yu, Xisen Wen, Flexural wave propagation in beams with periodically attached vibration absorbers: Band-gap behavior and band formation mechanisms, Journal of Sound and Vibration 332 (4) (2013) 867–893.

[12] Yong Xiao, Jihong Wen, Dianlong Yu, Xisen Wen, Flexural wave propagation in beams with periodically attached vibration absorbers: Band-gap behavior and band formation mechanisms, Journal of Sound and Vibration 332 (4) (2013) 867–893.

[13] Yong Xiao, Jihong Wen, Gang Wang, Xisen Wen, Theoretical and Experimental Study of Locally Resonant and Bragg Band Gaps in Flexural Beams Carrying Periodic Arrays of Beam-Like Resonators, Journal of Vibration and Acoustics 135 (4) (2013) 041006.

[14] Xiaoming Wang, Michael Yu Wang, An analysis of flexural wave band gaps of locally resonant beams with continuum beam resonators, Meccanica 51 (1) (2016) 171–178.

[15] Zuo Shuguang, Ni Tianxin, Wu Xudong, Fan Jialu, Studies of band gaps in flexural vibrations of a locally resonant beam with novel multi-oscillator configuration, Journal of Vibration and Control 23 (10) (2017) 1663–1674.

[16] Cheng Yang, Li Cheng, Suppression of bending waves in a beam using resonators with different separation lengths, The Journal of the Acoustical Society of America 139 (5) (2016) 2361–2371.

[17] Dianlong Yu, Yaozong Liu, Honggang Zhao, Gang Wang, Jing Qiu, Flexural vibration band gaps in Euler-Bernoulli beams with locally resonant structures with two degrees of freedom, Physical Review B 73 (6).

[18] Liao Liu, Mahmoud I. Hussein, Wave Motion in Periodic Flexural Beams and Characterization of the Transition Between Bragg Scattering and Local Resonance, Journal of Applied Mechanics 79 (1) (2012) 011003.

[19] YU Dianlong Wen Jihong Liu Yaozong, Qiu Jing Wang Gang, Flexural vibrations band gaps in periodic beams including rotary inertia and shear deformation effects, Chinese Journal of Mechanical Engineering 19 (1) (2006) 1.

[20] Yan Zhang, Zhi-Qiang Ni, Lin Han, Zi-Ming Zhang, Lin-Hua Jiang, Flexural vibrations band gaps in phononic crystal Timoshenko beam by plane wave expansion method, Optoelectronics and advanced materials - rapid communications 6 (11-12) (2012) 6.

[21] Yan Zhang, Zhi-Qiang Ni, Lin-Hua Jiang, Lin Han, Xue-Wei Kang, Study of the bending vibration characteristic of phononic crystals beam-foundation structures by Timoshenko beam theory, International Journal of Modern Physics B 29 (20) (2015) 1550136.

[22] L. Raghavan, A. Srikantha Phani, Local resonance bandgaps in periodic media: Theory and experiment, The Journal of the Acoustical Society of America 134 (3) (2013) 1950–1959.

[23] B. Sharma, C.T. Sun, Local resonance and Bragg bandgaps in sandwich beams containing periodically inserted resonators, Journal of Sound and Vibration 364 (2016) 133–146.

[24] Zhenyu Wang, Pei Zhang, Yongqiang Zhang, Locally Resonant Band Gaps in Flexural Vibrations of a Timoshenko Beam with Periodically Attached Multioscillators, Mathematical Problems in Engineering 2013 (2013) 1–10.

[25] Alf Søe-Knudsen, Design of stop-band filter by use of curved pipe segments and shape optimization, Structural and Multidisciplinary Optimization 44 (6) (2011) 863–874.

[26] S.V. Sorokin, O.A. Ershova, Plane wave propagation and frequency band gaps in periodic plates and cylindrical shells with and without heavy fluid loading, Journal of Sound and Vibration 278 (3) (2004) 501–526.

[27] Alexander Hvatov, Sergey Sorokin, Free vibrations of finite periodic structures in pass- and stop-bands of the counterpart infinite waveguides, Journal of Sound and Vibration 347 (2015) 200–217.

[28] F. Errico, M. Ichchou, S. De Rosa, O. Bareille, F. Franco, The modelling of the flow-induced vibrations of periodic flat and axial-symmetric structures with a wave-based method, Journal of Sound and Vibration 424 (2018) 32 – 47.

[29] E.D. Nobrega, F. Gautier, A. Pelat, J.M.C. Dos Santos, Vibration band gaps for elastic metamaterial rods using wave finite element method, Mechanical Systems and Signal Processing 79 (2016) 192–202. doi:10.1016/j.ymssp.2016.02.059.

[30] Hao Zhang, Yong Xiao, Jihong Wen, Dianlong Yu, Xisen Wen, Flexural wave band gaps in metamaterial beams with membrane-type resonators: theory and experiment, Journal of Physics D: Applied Physics 48 (43) (2015) 435305.

[31] C. W. Zhou, J. P. Lainé, M. N. Ichchou, A. M. Zine, Wave Finite Element Method Based on Reduced Model for One-Dimensional Periodic Structures, International Journal of Applied Mechanics 07 (02) (2015) 1550018.

[32] Elke Deckers, Stijn Jonckheere, Lucas Van Belle, Claus Claeys, Wim Desmet, Prediction of transmission, reflection and absorption coefficients of periodic structures using a hybrid wave based – finite element unit cell method, Journal of Computational Physics 356 (2018) 282 – 302.

[33] G. Trainiti, J.J. Rimoli, M. Ruzzene, Wave propagation in periodically undulated beams and plates, International Journal of Solids and Structures 75-76 (2015) 260–276.

[34] C.M. da Fonseca, On the eigenvalues of some tridiagonal matrices, Journal of Computational and Applied Mathematics 200 (1) (2007) 283 – 286.

[35] Young-Chung Hsue, Arthur J. Freeman, Ben-Yuan Gu, Extended plane-wave expansion method in three-dimensional anisotropic photonic crystals, Phys. Rev. B 72 (2005) 195118.

[36] A Geslain, S Raetz, M Hiraiwa, M Abi Ghanem, SP Wallen, A Khanolkar, N Boechler, J Laurent, C Prada, A Duclos, et al., Spatial laplace transform for complex wavenumber recovery and its application to the analysis of attenuation in acoustic systems, Journal of Applied Physics 120 (13) (2016) 135107.